Nanoscale

PAPER

View Article Online
View Journal | View Issue

Cite this: *Nanoscale*, 2023, **15**, 4361

Defect-assisted dynamic multicolor modulation in KLu_3F_{10}:Tb crystals for anti-counterfeiting†

Jianfeng Yang,[a] Yiheng Ping,[a] Hongping Ma*[a] and Lei Lei *[b]

Received 28th December 2022,
Accepted 26th January 2023

DOI: 10.1039/d2nr07264e

rsc.li/nanoscale

Excitation-dependent dynamic multicolor luminescent materials show potential for promising applications in the field of anti-counterfeiting. However, for most ultraviolet (UV)-excited lanthanide-doped materials, more than two types of activators are incorporated to realize multicolors. In this study, for the first time, KLu_3F_{10}:Tb crystals were used to realize excitation-dependent multicolor emissions. The morphology was modified by tuning the surface-coated citric acid (CA) content. During hydrothermal reactions, fluorine vacancy defects are formed on the crystal surface, and carboxyl groups (–COOH) are coated on the crystal surface to maintain the charge balance. Under 254 nm UV excitation, typical Tb^{3+} green emissions were observed, while a strong broadband emission peaking at 442 nm appeared in addition to these Tb^{3+} emissions under 365 nm excitation. The energy transfer (ET) process between the defect state and Tb^{3+} is clarified. This work may promote the development of single-type activator-doped multicolor luminescent materials for high-level anti-counterfeiting.

1. Introduction

Lanthanide-doped multicolor luminescent materials show potential for promising applications in anti-counterfeiting, temperature sensing, information encryption, flexible display, bio-detection and bio-imaging.[1–6] Several nanoparticles with designed core/shell structure have been used to realize excitation-dependent multicolor upconversion emissions.[7–11] For example, the emission color of $NaYF_4$:Yb/Ho/Ce@$NaYF_4$:Yb@$NaNdF_4$:Yb nanoparticles was changed from green to red upon switching the excitation wavelength from 808 nm to 980 nm;[12] the observed emission color of $NaGdF_4$:Yb/Tm@$NaGdF_4$@$NaYbF_4$:Nd@Na(Yb,Gd)F_4:Ho@$NaGdF_4$ nanoparticles was changed from green to blue when the excitation wavelength was tuned from 808 nm to 976 nm.[13] To avoid the use of expensive and dangerous lasers, several UV-excited downshifting materials were employed to control the emission colors. For example, the emission color of Ce/Tb co-doped $La_{9.33}(SiO_4)_6O_2$ changed from green to blue when the excitation wavelength changed from 229 nm to 315 nm;[14] and the output color of $Ca_2Ba_3(PO_4)_3Cl$:Ce/Tb exhibited green light under 229 nm excitation, but it was changed to cyan under 315 nm excitation.[15] In these systems, the green light originated from the characteristic transitions of Tb^{3+} activators, while the blue light originated from the characteristic emission of Ce^{3+} activators. It is important to develop new UV-excited multicolor materials for advanced applications.

Similar to the lanthanide activators, defects formed in the crystal structure can act as emitters to generate luminescence as well.[16–21] The defect luminescence has been reported in pure KRE_3F_{10} (RE = Sm–Lu, Y) nanocrystals. For example, for pure KY_3F_{10} nanocrystals prepared by a CA-assisted hydrothermal method, the strong broadband defect emission centered at 360 nm was recorded under 300 nm UV excitation.[22] Under excitation at 395 nm, KEu_3F_{10} nanocrystals exhibited a broadband emission centered at 460 nm.[23] However, the origin of defects and the corresponding mechanisms remain unclear. Moreover, inspired by the defect-related photoluminescence process, it is possible to realize dynamic multicolor emissions by incorporating activators into KRE_3F_{10} systems.

In this study, excitation-dependent multicolors are realized in KLu_3F_{10}:Tb crystals. Under 254 nm UV excitation, green emissions corresponding to the typical Tb^{3+}:$^5D_4 \rightarrow {}^7F_j$ (j = 6, 5, 4, and 3) transitions were observed. When the excitation wavelength was changed to 365 nm, a strong broadband emission peaking at 442 nm appeared in addition to the Tb^{3+} emissions. During crystal growth, fluorine vacancies are formed on the crystal surface, which then leads to broad defect luminescence. We further verified that this kind of multicolor product can be used for anti-counterfeiting.

[a]*School of Mechanical and Energy Engineering, Zhejiang University of Science and Technology, Hangzhou 310023, China. E-mail: hongpingma@163.com*
[b]*College of Optical and Electronic Technology, China Jiliang University, Hangzhou 310018, China. E-mail: leilei@cjlu.edu.cn*

† Electronic supplementary information (ESI) available. See DOI: https://doi.org/10.1039/d2nr07264e

2. Experimental

2.1. Synthesis

2.1.1. Materials. All raw chemicals including $Lu(NO_3)_3$ (99.9%), $Tb(NO_3)_3$ (99.9%), NH_4F, KOH, and CA were of analytical grade and used directly as received without further refinement. All of the above-mentioned materials were bought from Sigma Aldrich Company. Ethanol was supplied by Sinopharm Chemical Reagent Company.

2.1.2. Synthesis of KLu_3F_{10}:15Tb. A facile hydrothermal method was utilized to synthesize KLu_3F_{10}:15Tb. First, 0.85 mmol $Lu(NO_3)_3$ and 0.15 mmol $Tb(NO_3)_3$ were dissolved in 5 mL deionized water and 15 mL ethanol under vigorous stirring for 15 min. Second, 10 mL deionized water containing 5 mmol KOH, 3.5 mmol NH_4F and 1 mmol CA was added to this mixture and vigorously stirred for another 30 min. Finally, the resulting mixture was transferred to a hydrothermal reactor and held at 200 °C for 12 h. The products were washed several times with distilled water and ethanol and dried at 60 °C for 3 h. The other samples studied in this work were synthesized by a similar method.

2.2. Sample characterizations

X-ray diffraction (XRD) patterns of the samples were acquired using a powder diffractometer (Bruker D8 Advance) with Cu-Kα (λ = 1.5405 A) radiation. XRD patterns were recorded in the 2(θ) range of 10° to 80° at a scan rate of 0.02°. The morphology and size of the products were observed using a scanning electron microscope (SEM, FEI Tecnai G2 F20) equipped with an energy-dispersive X-ray spectrometer (EDX, Aztec X-Max 80T). Luminescence spectra and decay curves of the samples were recorded using a fluorescence spectrometer-Fluorolog (Jobin Yvon FL3-211).

3. Results and discussion

As shown in Fig. 1a, the XRD patterns of the KLu_3F_{10} and KLu_3F_{10}:15Tb products are well indexed to the standard data of pure cubic phase KYb_3F_{10} (JCPDS no. 27-0462). The XRD peaks shift toward a low angle after doping Tb^{3+} ions, which is owing to the larger ionic radius of Tb^{3+} (r = 0.858 nm) than that of Lu^{3+} (r = 0.848 nm).[24] These results also indicate that Tb^{3+} was successfully incorporated into the host without the emergence of extra impurities.[25] Furthermore, since the particle size of KLu_3F_{10} (~1 μm) is smaller than that of KLu_3F_{10}:15Tb (~4 μm), the XRD diffraction peaks become narrower after the incorporation of Tb^{3+}.[26] The products prepared with different CA contents and reaction temperatures were also pure phases (Fig. S1 and S2†). The morphology of the

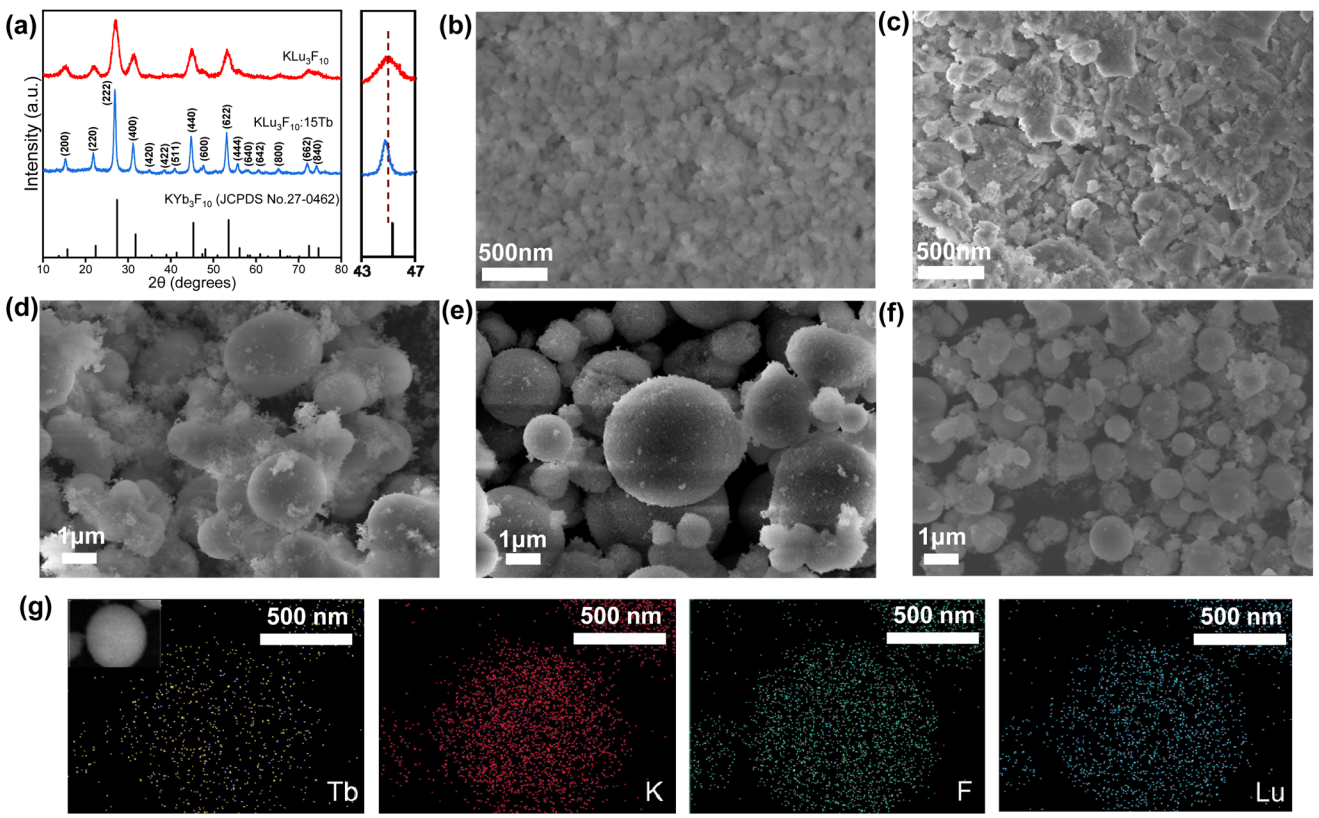

Fig. 1 (a) XRD patterns of the KLu_3F_{10} and KLu_3F_{10}:15Tb products. SEM images of the KLu_3F_{10}:15Tb products prepared without CA (b), and with 0.3 mmol CA (c), 0.6 mmol CA (d) and 1 mmol CA (e) addition. SEM image (f) and EDX mapping results (g) of the KLu_3F_{10}:15Tb products prepared at 170 °C.

KLu_3F_{10}:15Tb product was tuned by adjusting the CA content and reaction temperature. As shown in Fig. 1b, the average particle size of the product without the addition of CA surfactants was about 100 nm. As the CA content increased from 0.3 mmol to 1 mmol, the average particle size increased from ~300 nm to ~4 μm, and the shape changed from irregular to spherical (Fig. 1c–e). When the reaction temperature was decreased from 200 to 170 °C, the average particle size reduced from ~4 to ~1 μm (Fig. 1f). The energy-dispersive X-ray spectrum suggested the existence of K, Lu, F and Tb elements in the final product (Fig. S3†), and the EDX mapping results further revealed the uniform distribution of these elements in a single particle (Fig. 1g).[27]

As shown in Fig. 2a, with monitoring the 545 nm emission of KLu_3F_{10}:Tb, a broad photoluminescence excitation (PLE) spectrum corresponding to the defect transition[28] as well as few sharp peaks corresponding to the Tb^{3+}:4f–4f transitions were observed. With monitoring the 442 nm emission, only a broad PLE spectrum in the range of 270–400 nm was recorded. Under 254 nm UV excitation, photoluminescence (PL) peaks at 487 nm, 545 nm, 585 nm and 622 nm were assigned to the Tb^{3+}:$^5D_4 \rightarrow {}^7F_j$ (j = 6, 5, 4, and 3) transitions.[29] When the excitation wavelength was changed to 365 nm, the intensity of the four characteristic emissions was significantly enhanced. Moreover, a strong broadband emission peaking at 442 nm was observed (Fig. 2b). By fitting the decay curve with a tri-exponential function,[30–32] the lifetime of 442 nm was calculated to be 7.93 ns, while that of Tb^{3+}:$^5D_4 \rightarrow {}^7F_5$ (545 nm) was calculated to be 6.06 ms (Fig. 2c and d). The nanosecond lifetime is consistent with the electron's transition in the defect state.[33,34] To clarify the origin of this broad emission, pure KLu_3F_{10} crystals were prepared and studied. Under 365 nm excitation, the broad PL emission at 442 nm was also recorded (Fig. 2e). Furthermore, this PL intensity was greatly decreased after annealing at high temperatures. In particular, after annealing at 500 °C, the broad PL fully disappeared (Fig. 2f). These results indicated that the broad PL originated from the defects formed on the surface of the crystals.[35,36]

To further clarify the mechanism for the above-mentioned defect luminescence, the optical properties of KLu_3F_{10}:Tb crystals prepared with different CA contents and at different reaction temperatures and times were studied. As shown in Fig. 3a, when the CA content was less than 0.3 mmol, only typical Tb^{3+} emissions were observed. With increase in CA content to 0.6 mmol, both emissions from Tb^{3+} and defects were observed. This result suggests that the defect is highly related to the surface CA content. As shown in Fig. 3b–d, with the decrease in the reaction temperature and increase in reaction time, the defect PL intensity was enhanced. Based on these results, a possible mechanism for the formation of defects was schematically illustrated in Fig. 3e. During the crystal growth, fluorine vacancies are formed on the crystal surface. Negatively charged –COOH is coated on the surface to maintain the

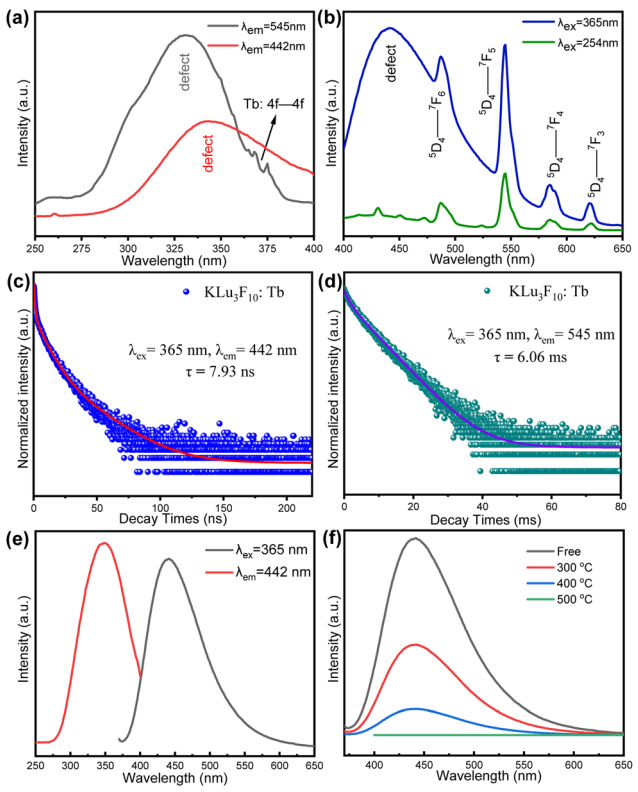

Fig. 2 (a) PLE and (b) PL spectra of KLu_3F_{10}:Tb. Decay curves of the 442 nm (c) and 545 nm (d) emissions. (e) PLE and PL spectra of pure KLu_3F_{10}. (f) PL spectra of KLu_3F_{10} annealed at different temperatures (free; 300 °C, 3 h; 400 °C, 3 h; 500 °C, 3 h).

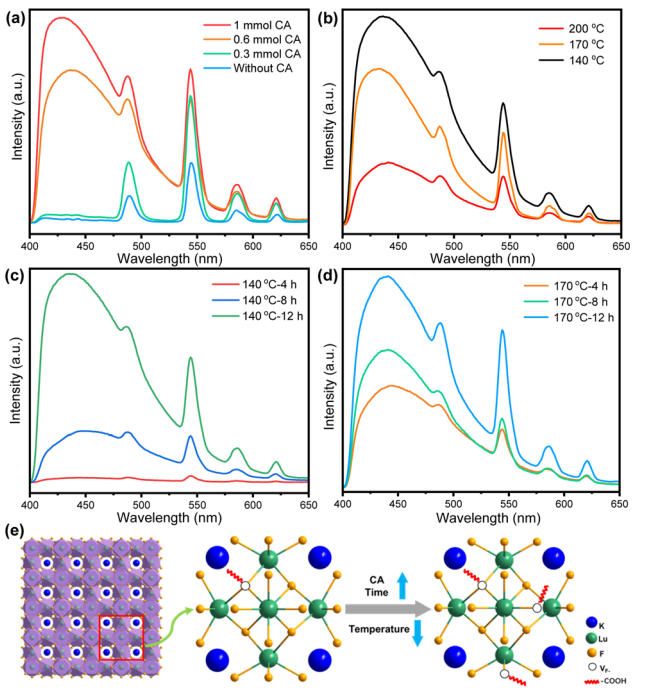

Fig. 3 PL spectra of KLu_3F_{10}:15Tb synthesized with different CA contents (a), different reaction temperatures (b), different hydrothermal reaction times at 140 °C (c) and 170 °C (d). (e) Schematic illustration of the proposed defect formation mechanism.

charge balance. The fluorine vacancies play a role as defect levels to capture electrons, which then leads to defect luminescence. With the decrease in the reaction temperature or increase in the reaction time and CA, the amount of fluorine vacancy and surface coated –COOH increases. As a result, the defect luminescence enhances as well.

To reveal the possible ET process between the defects and Tb^{3+} activators, the temperature-dependent optical properties of KLu_3F_{10}:15Tb were studied. As shown in Fig. 4a and b, with the increase in temperature from 303 to 483 K, the emission intensities of the defects and Tb^{3+} showed similar decreasing trends. In addition, with the increase in Tb^{3+} doping concentration, the emission intensity at 545 nm increased gradually, while the defect luminescence at 442 nm decreased gradually (Fig. 4c). The calculated average lifetimes of the defect luminescence decreased from 8.83 ns, 8.3 ns, to 7.89 ns with the increase in Tb^{3+} concentration from 10, 15 to 20 mmol%, respectively (Fig. 4d–f). These results manifest the existence of ET between the defect states and the Tb^{3+} excited state. A possible PL mechanism for the excitation-dependent multicolor is shown in Fig. 4g. Under 254 nm UV excitation, the electrons are excited from the ground state ($4f^8$) to the excited state ($4f^75d$), then the $^5D_3$ and $^5D_4$ energy levels are populated *via* non-radiative relaxation.[37] Strong green emissions are produced *via* $^5D_4$–^7F_j (j = 3–6) transitions. When the excitation wavelength is changed to 365 nm, the UV input photons are first absorbed by the defects, leading to intense blue emissions. Meanwhile, part of the energy is transferred from the

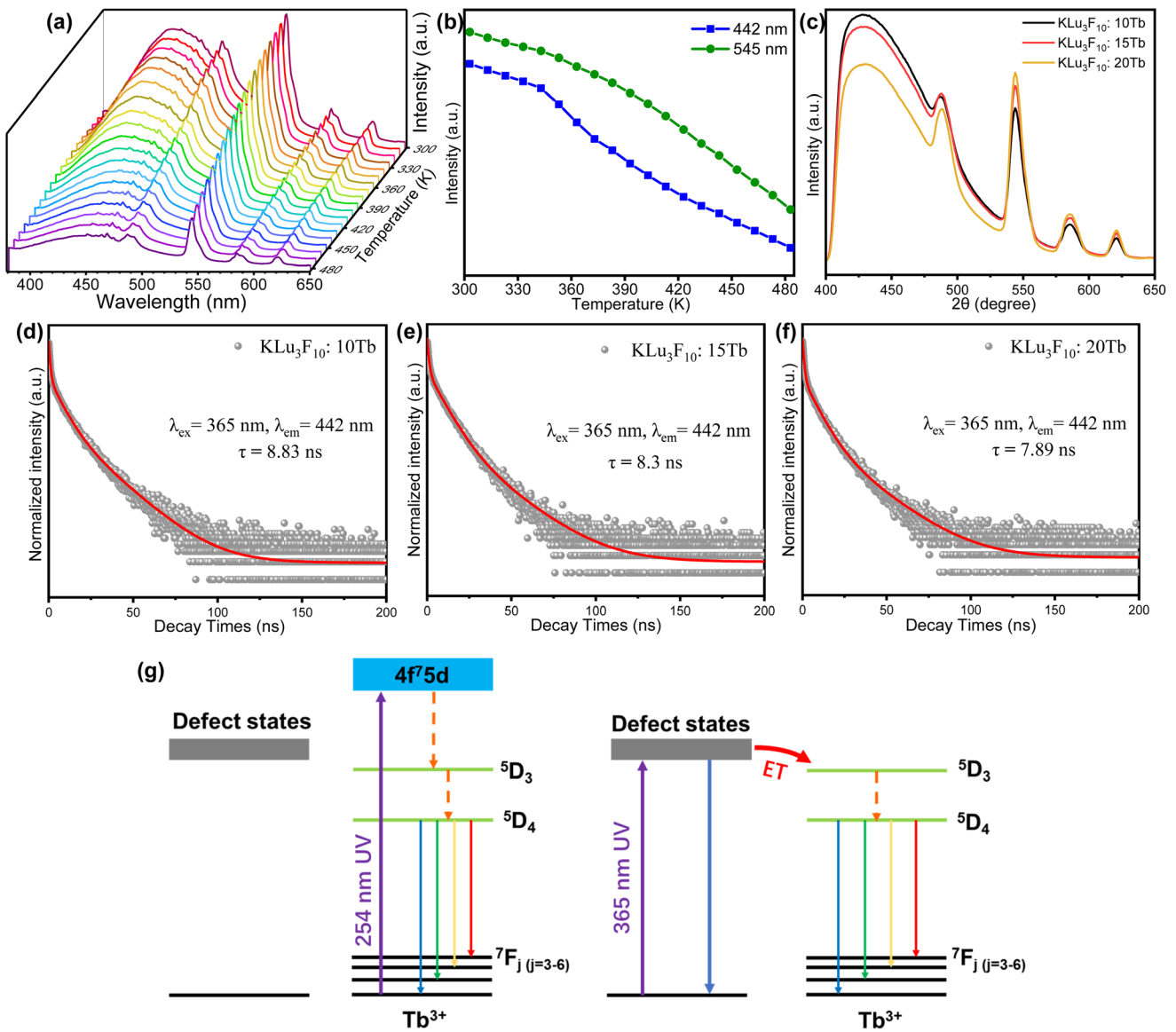

Fig. 4 (a) PL spectra of KLu_3F_{10}:15Tb excited at 365 nm under 303–483 K. (b) Variation trend of luminescence intensity at 442 nm and 545 nm under 303–483 K. (c) PL spectra of KLu_3F_{10}:xTb (x = 10, 15, and 20). Decay curves of (d) KLu_3F_{10}:10Tb, (e) KLu_3F_{10}:15Tb and (f) KLu_3F_{10}:20Tb at 442 nm. (g) Proposed excitation-dependent PL mechanism.

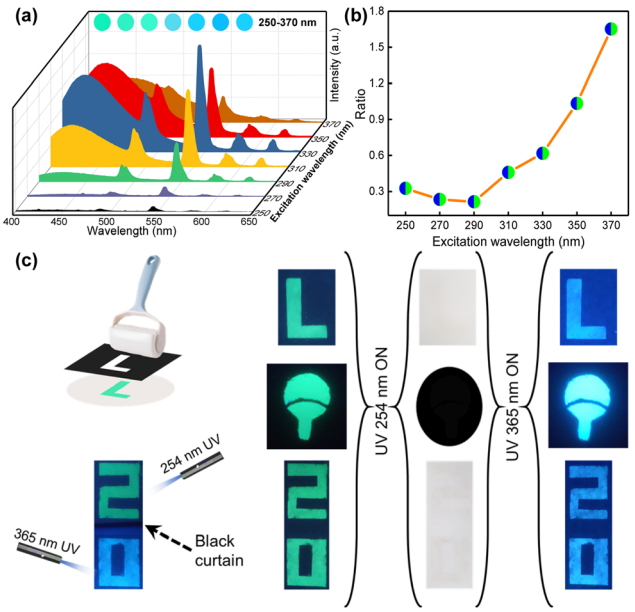

Fig. 5 (a) PL spectra of KLu_3F_{10}:15Tb under 250–370 nm excitation. (b) Corresponding luminescence intensity ratio of 442 nm to 545 nm. (c) Screen printing process and luminous patterns irradiated by 254 nm and 365 nm UV lamps (6 W).

defect state to the Tb^{3+}:$^5D_3$ energy level, which leads to green emissions.[38]

As shown in Fig. 5a, the emission color of KLu_3F_{10}:15Tb can be changed from green to bright cyan by adjusting the excitation wavelength. The shift in luminescent color can also be observed clearly in the International Commission on Illumination (CIE) chromaticity diagram of KLu_3F_{10}:15Tb (yellow arrow in Fig. S4†). We calculated the ratio of the emission intensity at 442 nm and 545 nm for different wavelength excitations (Fig. 5b). The ratio decreases as the excitation wavelength increases from 250 nm to 290 nm, but increases with the further increase in excitation wavelength to 370 nm. The change in the ratio of the two emission peaks leads to a change in the final luminescence color of the product. To demonstrate the effectiveness of KLu_3F_{10}:15Tb in practical anti-counterfeiting applications, we used KLu_3F_{10}:15Tb to prepare the letter "L", the number "20" and circular sector patterns by screen printing technology. The color of these patterns changed significantly when the excitation wavelength was changed from 254 nm to 365 nm (Fig. 5c). These results indicate that the present studied KLu_3F_{10}:Tb crystals are potential candidates for anti-counterfeiting labels.

4. Conclusion

In summary, single Tb^{3+}-doped KLu_3F_{10} crystals prepared by a hydrothermal method exhibited excitation-dependent dynamic multicolor variations. We verified that fluorine vacancies are formed on the crystal surface and –COOH groups are coated on the crystal surface to maintain the charge balance during the hydrothermal reaction. Under 254 nm UV excitation, typical Tb^{3+} green emissions were observed, while a strong broadband emission peaking at 442 nm appeared in addition to these Tb^{3+} emissions under 365 nm excitation. The broad band emission originated from the electron transition in the defects. Moreover, the energy transfer from the defect state to Tb^{3+} is clarified. We further verified that this kind of material can be used for anti-counterfeiting labels. Our results may promote the development of single-type activator-doped multicolor luminescent materials for high-level anti-counterfeiting applications.

Conflicts of interest

There are no conflicts to declare.

Acknowledgements

This work was supported by the Zhejiang Provincial Natural Science Foundation of China (no. LZ20E020001, no. LZ21A040002), the National Natural Science Foundation of China (no. 61875176, 52172164).

References

1 J. Xu, B. Zhang, L. Jia, Y. Fan, R. Chen, T. Zhu and B. Liu, *ACS Appl. Mater. Interfaces*, 2019, **11**, 35294–35304.
2 Y. Liu, G. Bai, Y. Lyu, Y. Hua, R. Ye, J. Zhang, L. Chen, S. Xu and J. Hao, *ACS Nano*, 2020, **14**, 16003–16012.
3 Y. Zhu, X. Li, Z. Guo, H. Sun, Q. Zhang and X. Hao, *J. Am. Ceram. Soc.*, 2020, **103**, 3205–3216.
4 M. Yu, Y. Chen, Y. Luo, G. Gong, Y. Zhang, H. Tan, L. Xu and J. Xu, *React. Funct. Polym.*, 2022, **178**, 105350.
5 S. K. Ray, B. Joshi, S. Ramani, S. Park and J. Hur, *J. Alloys Compd.*, 2022, **892**, 162101.
6 J. Wang, Y. Zhu, C. A. Grimes and Q. Cai, *Nanoscale*, 2019, **11**, 12497–12501.
7 L. Lei, Y. Wang, W. Xu, R. Ye, Y. Hua, D. Deng, L. Chen, P. N. Prasad and S. Xu, *Nat. Commun.*, 2022, **13**, 5739.
8 L. Lei, Y. Wang, A. Kuzmin, Y. Hua, J. Zhao, S. Xu and P. N. Prasad, *eLight*, 2022, **2**, 17.
9 H. Dong, L. D. Sun, W. Feng, Y. Gu, F. Li and C. H. Yan, *ACS Nano*, 2017, **11**, 3289–3297.
10 P. Hu, S. Zhou, Y. Wang, J. Xu, S. Zhang and J. Fu, *Chem. Eng. J.*, 2022, **431**, 133728.
11 F. Lin, Z. Sun, M. Jia, A. Zhang, Z. Fu and T. Sheng, *J. Lumin.*, 2020, **218**, 116862.
12 X. Fu, S. Fu, Q. Lu, J. Zhang, P. Wan, J. Liu, Y. Zhang, C. H. Chen, W. Li, H. Wang and Q. Mei, *Nat. Commun.*, 2022, **13**, 4741.
13 H. Wen, H. Zhu, X. Chen, T. F. Hung, B. Wang, G. Zhu, S. F. Yu and F. Wang, *Angew. Chem., Int. Ed.*, 2013, **52**, 13419–13423.

14 C. Peng, M. Shang, G. Li, Z. Hou, D. Geng and J. Lin, *Dalton Trans.*, 2012, **41**, 4780.
15 M. Shang, D. Geng, D. Yang, X. Kang, Y. Zhang and J. Lin, *Inorg. Chem.*, 2013, **52**, 3102–3112.
16 C. Zhang and J. Lin, *Chem. Soc. Rev.*, 2012, **41**, 7938–7961.
17 Y. K. Jung, J. Calbo, J. S. Park, L. D. Whalley, S. Kim and A. Walsh, *J. Mater. Chem. A*, 2019, **7**, 20254–20261.
18 M. A. Reshchikov and H. Morkoç, *J. Appl. Phys.*, 2005, **97**, 061301.
19 A. Kar, S. Kundu and A. Patra, *J. Phys. Chem. C*, 2011, **115**, 118–124.
20 T. P. Mokoena, Z. P. Tshabalala, K. T. Hillie, H. C. Swart and D. E. Motaung, *Appl. Surf. Sci.*, 2020, **525**, 146002.
21 E. Mitterreiter, B. Schuler, A. Micevic, D. Hernangómez-Pérez, K. Barthelmi, K. A. Cochrane, J. Kiemle, F. Sigger, J. Klein, E. Wong, E. S. Barnard, K. Watanabe, T. Taniguchi, M. Lorke, F. Jahnke, J. J. Finley, A. M. Schwartzberg, D. Y. Qiu, S. Refaely-Abramson, A. W. Holleitner, A. Weber-Bargioni and C. Kastl, *Nat. Commun.*, 2021, **12**, 3822.
22 Q. Cui and J. Xu, *J. Mater. Sci.: Mater. Electron.*, 2016, **27**, 4372–4377.
23 C. Li, Z. Xu, D. Yang, Z. Cheng, Z. Hou, P. a. Ma, H. Lian and J. Lin, *CrystEngComm*, 2012, **14**, 670–678.
24 D. Xu, A. Li, L. Yao, H. Lin, S. Yang and Y. Zhang, *Sci. Rep.*, 2017, **7**, 43189.
25 G. Amira, B. Chaker and E. Habib, *Spectrochim. Acta, Part A*, 2017, **177**, 164–169.
26 R. Yogamalar, R. Srinivasan, A. Vinu, K. Ariga and A. C. Bose, *Solid State Commun.*, 2009, **149**, 1919–1923.
27 Y. Cheng, L. Lei, W. Zhu, Y. Wang, H. Guo and S. Xu, *Nano Res.*, 2022, DOI: **10.1007/s12274-022-4998-7**.
28 N. Mendelson, D. Chugh, J. R. Reimers, T. S. Cheng, A. Gottscholl, H. Long, C. J. Mellor, A. Zettl, V. Dyakonov, P. H. Beton, S. V. Novikov, C. Jagadish, H. H. Tan, M. J. Ford, M. Toth, C. Bradac and I. Aharonovich, *Nat. Mater.*, 2020, **20**, 321–328.
29 S. Singh and D. Singh, *Rare Met.*, 2020, **40**, 3289–3298.
30 S. Mukherjee, N. Pathak, D. Das and D. Dutta, *RSC Adv.*, 2021, **11**, 5815–5831.
31 Y. Fujimoto, K. Saeki, T. Yanagida, M. Koshimizu and K. Asai, *Radiat. Meas.*, 2017, **106**, 151–154.
32 K. Jiang, Y. Wang, X. Gao, C. Cai and H. Lin, *Angew. Chem., Int. Ed.*, 2018, **57**, 6216–6220.
33 M. Fujimaki, Y. Ohki and H. Nishikawa, *J. Appl. Phys.*, 1997, **81**, 1042–1046.
34 C. K. Lin, Y. Luo, H. You, Z. Quan, J. Zhang, J. Fang and J. Lin, *Chem. Mater.*, 2005, **18**, 458–464.
35 Y. Ji, X. Liu, B. Li, J. Zhang and X. Wang, *J. Lumin.*, 2014, **146**, 150–156.
36 W. Q. Peng, S. C. Qu, G. W. Cong and Z. G. Wang, *Mater. Sci. Semicond. Process.*, 2006, **9**, 156–159.
37 X. Li, Y. Zhang, D. Geng, J. Lian, G. Zhang, Z. Hou and J. Lin, *J. Mater. Chem. C*, 2014, **2**, 9924–9933.
38 Y. Xie, Z. Ma, L. Liu, Y. Su, H. Zhao, Y. Liu, Z. Zhang, H. Duan, J. Li and E. Xie, *Appl. Phys. Lett.*, 2010, **97**, 141916.